Using the inverse finiteelement method to harmonise classical modal analysis with fibreoptic strain data for robust populationbased structural health monitoring

Received: 4 October 2023 | Revised: 9 March 2024 | Accepted: 6 May 2024

DOI: 10.1111/str.12481

RESEARCH ARTICLE

strain WILEY

Using the inverse finite-element method to harmonise classical modal analysis with fibre-optic strain data for robust population-based structural health monitoring

Giulia Delo[1] | **Rinto Roy**[2] | **Keith Worden**[3] | **Cecilia Surace**[2]

[1]Department of Mechanical and Aerospace Engineering, Politecnico di Torino, Turin, Italy

[2]Department of Structural, Geotechnical and Building Engineering, Politecnico di Torino, Turin, Italy

[3]Dynamics Research Group, Department of Mechanical Engineering, University of Sheffield, Shefleld, UK

Correspondence
Giulia Delo, Department of Mechanical and Aerospace Engineering, Politecnico di Torino, Corso Duca degli Abruzzi, 24, Turin 10129, Italy.
Email: giulia.delo@polito.it

Funding information
UK Engineering and Physical Sciences Research Council (EPSRC), Grant/Award Numbers: EP/S001565/1, EP/W005816/1

Abstract

Vibration-based approaches to structural health monitoring (SHM) gained increasing significance for assessing the behaviour of existing structures because of their non-intrusive nature and high sensitivity to damage. However, data availability often limits the application of SHM approaches. The population-based structural health monitoring (PBSHM) theory addresses this challenge, enhancing diagnostic inferences by sharing knowledge across a population of similar structures. In real-life scenarios, sharing data from distinct structures requires dealing with results obtained with different experimental setups, multiple sensors, input choices and acquisition systems. Therefore, it is crucial to harmonise various features to achieve accurate and reliable results. The present study presents the results of a classic experimental modal analysis (EMA) using scanning laser Doppler vibrometer (SLDV) measurements and a strain-based EMA conducted using high-definition distributed fibre-optic strain sensors. The experimental case study of a laboratory-scale steel aircraft subjected to specific operating and damage conditions is introduced, allowing for a comprehensive discussion of the features extracted from the two EMA techniques, which can also be generalised to structures within different domains. This research highlights the advantages and limitations of fibre-optic-based EMA compared to classic methods, as fibre-optic strain sensors offer a cost-effective alternative to accelerometers or SLDV for dynamic testing. Furthermore, the feasibility of employing the inverse finite-element method (iFEM) in the dynamic domain is investigated. This method can estimate the whole displacement field of a structure from a limited number of strain values, thus harmonising strain measurements with the SLDV measurements. By analysing the features extracted from different EMA techniques within the PBSHM framework, this study contributes to advancing the understanding and application of the PBSHM approach in diverse experimental scenarios, laying the foundation for further investigation of features and adequate methods for sharing damage-state knowledge across a population of structures.

KEYWORDS

fibre-optic sensors, inverse finite-element method (iFEM), population-based structural health monitoring (PBSHM), strain experimental modal analysis

1 | INTRODUCTION

Structural health monitoring (SHM) has gained significant interest in recent decades, with a variety of methods proposed to investigate existing structures and identify damage. Among these, vibration-based methods are highly applicable because of their non-intrusive nature and ability to detect structural issues with high sensitivity. Despite the increase in the types of sensors suitable for SHM purposes, the available data for specific case studies are often insufficient to guarantee a robust performance of most SHM approaches, as highlighted by Gardner et al.[1] To address this challenge, the theory of population-based structural health monitoring (PBSHM) has been introduced, to facilitate knowledge-transfer between source and target structures, which should be sufficiently similar to each other.[2–4] Within this framework, it is necessary to address the inconsistencies between heterogeneous structural domains. Additionally, sharing data from distinct structures in real cases often requires analysing the results obtained with different experimental setups, sensors, input choices and acquisition systems. This issue highlights the importance of comparing and standardising various features and investigating ways of achieving accurate and reliable results despite varying experimental techniques. Thus, this study compares the results of a classic experimental modal analysis (EMA), performed via scanning laser Doppler vibrometer (SLDV) measurements and a strain EMA, performed via high-definition distributed fibre-optic strain sensors. The main objective is to investigate which features can be extracted and how they can be harmonised to facilitate their integration into the PBSHM framework. Accordingly, implementing an appropriate knowledge-sharing approach will be the subject of future progress in this study. The experimental case study of a steel aeroplane laboratory structure is analysed. As a first investigation, the two different EMA approaches are evaluated on the same system, adopting the same operating and damage conditions. This is used to analyse the features that can be extracted in a homogeneous population and afterwards extend it to heterogeneous populations.

The study focusses on fibre-optic-based EMA against more classic methods. Fibre-optic strain sensors are a cost-effective alternative to accelerometers or SLDV for dynamic testing. These sensors are examined because they can measure strains at a dense set of points in a structure, providing valuable insights into the local behaviour of specific components or regions. In addition, a dense set of measurements could similarly be achieved using the SLDV. However, each point would be measured separately, while the fibre-optic measurements are contemporary and thus considerably faster; compared to accelerometers, they are minimally intrusive. Additionally, high-resolution strain measurements can be highly sensitive to small variations in natural frequencies, damping ratios and mode shapes.[5] Moreover, fibre-optic sensors offer flexibility in configurations and test setups, and they can be installed on structures of various geometries, including complex or irregular shapes. Thus, these sensors provide further insight for monitoring structures in localised areas or where other sensors would be difficult to mount or access. They can also be applied to monitor structural behaviour during operations, such as in-flight, as opposed to SLDV, which is more efficient in the laboratory environment.

Given the strain measurements along the sensor's axis, this paper proposes the application of the inverse finite-element method (iFEM)[6] for harmonising the results, aiding the comparison with the displacements extracted from the SLDV. The iFEM approach enables the determination of displacements and strains throughout the structure from a limited number of strain measures, providing valuable insights into its mechanical behaviour. This study extends the use of iFEM to investigate the dynamic behaviour of structures, by illustrating how iFEM can be combined with strain-based EMA for the reconstruction of displacement frequency response functions (FRFs) and the identification of modal parameters.

This case study is part of a broader population of similar structures, which mainly follows the geometry of the benchmark study conducted by the Structures and Materials Action Group (SM-AG19) of the Group for Aeronautical Research Technology in EURope (GARTEUR).[7,8] The heterogeneity of the population results from designing models of different materials and geometric dimensions, creating a comprehensive dataset to investigate the potentialities of PBSHM in the aerospace field.

The layout of the paper is as follows: Section 2 presents the methods to perform the two EMAs and describes the iFEM strategy for mode-shape sensing. Section 3 illustrates the case study of the Garteur aeroplane's dynamic response

in undamaged and damaged conditions. The results obtained from the two EMA approaches are presented, and the extracted features are compared in Section 4. Subsequently, some discussions and conclusions are provided.

2 | METHODS

2.1 | EMA: Comparison between strain and classical approaches

EMA is frequently adopted as a method for extracting the modal parameters of a test structure.[9] In this study, a classic EMA is performed adopting SLDV, which can provide operating deflection shapes of an entire surface and transfer functions. In addition, a strain EMA is contemporarily performed.

Strain modal analysis has been proposed as a particular EMA approach.[10,11] Several strain gauges can be used. Among these, fibre-optic sensors are widely employed, because of their small physical size, insensitivity to electromagnetic interference, light weight and the possibility to be used at high temperatures or in environmentally unfavourable conditions.[12] In addition, Yam et al. stated that the strain mode shapes (SMSs) are more sensitive to localised changes than the displacement mode shapes (DMSs),[5] and Davis et al. used fibre-optic sensors for mode-shape identification.[13]

Ling et al. proposed a more comprehensive study of dynamic strain measurements[14]; they measured the dynamic strain response of a clamped-clamped composite beam via embedded fibre Bragg grating (FBG) sensors, in undamaged and damaged conditions (i.e., delamination), and used these measurements to compute the SMSs, exploiting the simplicity of the test structure. This study confirmed how FBG sensors can be used for dynamic measurements and also damage detection, because SMSs show higher sensitivity to delamination rather than the natural frequencies, especially when the damage is small and localised. Indeed, the shift in natural frequencies caused by delamination is not sufficiently accurate to be used alone for identifying damage, since changes in operational or environmental conditions could produce the same effect. Paolozzi and Gasbarri also proposed the use of fibre-optic sensors for dynamic SHM purposes, focussing on the analysis of strain frequency response functions (SFRFs) and SMSs.[15]

The steady-state response of a viscously damped dynamical system can be written in terms of its modal parameters as[9]

$$\mathrm{X}(\omega) = \Phi \left[\backslash \omega_r^2 - \omega^2 + 2i\zeta_r \omega \omega_r \backslash \right]^{-1} \Phi^{\mathrm{T}} \mathrm{F}(\omega) = \mathrm{H}(\omega)\mathrm{F}(\omega), \tag{1}$$

where Φ is the matrix of mass-normalised DMSs; ω_r and ζ_r are the natural frequency and the viscous damping ratio of the rth mode, respectively; $[\backslash\ \backslash]$ represents a diagonal matrix; $\mathbf{H}(\omega)$ is the receptance matrix; and $\mathbf{F}(\omega)$ is the excitation force vector.

The corresponding system response in terms of strains obtained from Equation 1 has the form[16]

$$\mathbf{X}^{\varepsilon}(\omega) = \Phi^{\varepsilon} \left[\backslash \omega_r^2 - \omega^2 + 2i\zeta_r \omega \omega_r \backslash \right]^{-1} \Phi^{\mathrm{T}} \mathrm{F}(\omega) = \mathbf{H}^{\varepsilon}(\omega)\mathrm{F}(\omega)\,, \tag{2}$$

where Φ^{ε} is the matrix of mass-normalised SMSs and $\mathbf{H}^{\varepsilon}$ is the matrix of SFRFs. $\mathbf{H}^{\varepsilon}$ is defined in terms of the matrix of strain modal constants, ${}_r\mathbf{A}^{\varepsilon} = \Phi^{\varepsilon}\Phi_r$, and can be written as

$$\mathbf{H}^{\varepsilon}(\omega) = \sum_{r=1}^{n} \frac{{}_r\mathbf{A}^{\varepsilon}}{\omega_r^2 - \omega^2 + 2i\zeta_r \omega \omega_r}. \tag{3}$$

The steps for performing strain EMA are similar to the ones required for the classical analysis. The main difference is that SMSs cannot be mass-normalised only using strain results.[10] However, the normalisation can be aided by the classical EMA,[11] using one direct motion FRF. In this framework, most research case studies concern simple beams or plates, for which it is possible to easily study the strain response and extract the mode shapes.[11,13,14,16,17] In this study, a

more complex laboratory-scale structure is investigated, that is, a steel Garteur aeroplane. Additionally, iFEM is used in this work as a novel approach for mode-shape sensing.

2.2 | Mode-shape sensing using iFEM

Shape sensing is defined as the inverse problem of estimating structural displacements from discrete in-flight surface strains,[6,18] and its solution approaches offer an efficient means of developing real-time monitoring systems for aerospace structures. iFEM is such a variationally based shape-sensing method proposed by Tessler and Spangler,[19,20] with a key advantage of being independent of the material properties or operational conditions of the structure (and avoids uncertainties of model-based approaches). Although iFEM has been demonstrated for a variety of complex statically loaded structures,[21] it is of interest to extend investigations to dynamic responses in the field of EMA. In particular, this study aims to use iFEM as a tool for mode-shape sensing. But first, the theoretical foundation of iFEM is briefly discussed below.

The iFEM formulation for plates or shell structures is based on the kinematic assumptions of Mindlin plate theory. Considering a plate of thickness $2t$, the Cartesian components of the displacement vector can be expressed in terms of the kinematic variables u, v, w, θ_x and θ_y associated with the plate midplane (x, y) as[22]:

$$\begin{aligned} u_x(x,y,z) &= u(x,y)+z\theta_y(x,y), \\ u_y(x,y,z) &= v(x,y)-z\theta_x(x,y), \\ u_z(x,y,z) &= w(x,y), \end{aligned} \tag{4}$$

where u and v are the displacements in the x and y directions, w is the average transverse deflection and θ_x and θ_y are the rotations about the x and y axes.

Using the linear strain-displacement relations, the strain field of the plate is expressed in terms of eight strain measures given by

$$\begin{aligned} \mathbf{e} &= \{u_{,x}, v_{,y}, u_{,y}+v_{,x}\}', \\ \mathbf{k} &= \{\theta_{y,x}, -\theta_{x,y}, -\theta_{x,x}+\theta_{y,y}\}', \\ \mathbf{g} &= \{w_{,x}+\theta_y, w_{,y}-\theta_x\}' \end{aligned} \tag{5}$$

where $\mathbf{e}$, $\mathbf{k}$ and $\mathbf{g}$ are the vectors of strain measures corresponding to the in-plane stretching, bending and transverse shear deformation of the midplane, respectively, and $'$ indicates the transpose of a vector or matrix.

iFEM uses the finite-element framework to discretise the structure and approximates the strain measures within each element by interpolating the nodal degrees of freedom, $\mathbf{u}^e$, using shape functions. Key to the iFEM formulation is the use of a functional representing the weighted-least-squares error between the experimentally measured strains and those coming from the finite-element approximations. For each inverse element, this error functional, Φ^e, is given by

$$\Phi^e(\mathbf{u}^e) \equiv \mathbf{w}_e \|\mathrm{e}(\mathbf{u}^e) - \mathbf{e}^\varepsilon\|^2 + \mathbf{w}_k \|\mathrm{k}(\mathbf{u}^e) - \mathbf{k}^\varepsilon\|^2 + \mathbf{w}_g \|\mathrm{g}(\mathbf{u}^e) - \mathbf{g}^\varepsilon\|^2, \tag{6}$$

where $\mathbf{w}_e$, $\mathbf{w}_k$ and $\mathbf{w}_g$ are row vectors of weighting coefficients used to enforce the correlation between the experimental and analytical quantities and $\mathbf{e}^\varepsilon$, $\mathbf{k}^\varepsilon$ and $\mathbf{g}^\varepsilon$ are the strain measures computed from experimental strain measurements.

In the case of a plate structure instrumented with strain sensors at any point (x_i, y_i) on the top $(+)$ and bottom $(-)$ surfaces, $\mathbf{e}^\varepsilon$ and $\mathbf{k}^\varepsilon$ can be computed from the surface strain measurements (ε_{xx}, ε_{yy} and γ_{xy}) using the relations

$$\mathbf{e}_i^e = \frac{1}{2}\left\{\left(\varepsilon_{xx}^+ + \varepsilon_{xx}^-\right), \left(\varepsilon_{yy}^+ + \varepsilon_{yy}^-\right), \left(\gamma_{xy}^+ + \gamma_{xy}^-\right)\right\}_i',$$
$$\mathbf{k}_i^e = \frac{1}{2t}\left\{\left(\varepsilon_{xx}^+ - \varepsilon_{xx}^-\right), \left(\varepsilon_{yy}^+ - \varepsilon_{yy}^-\right), \left(\gamma_{xy}^+ - \gamma_{xy}^-\right)\right\}_i' \quad (7)$$

The experimental transverse shear $\mathbf{g}^e$ cannot be determined directly from the surface strain measurements. Additionally, this contribution is typically negligible in comparison to the bending one, especially for analysing thin plates.[20] Thus, the third term in Equation (6) is replaced by an L_2 squared norm of the analytical transverse shear strain measures, and the corresponding weighting coefficient is set to a small value ($\mathbf{w}_g = 10^{-5}$). Minimising the element error functional, Φ^e, with respect to the unknown nodal degrees of freedom, $\mathbf{u}^e$, leads to a set of linear algebraic equations, $\mathbf{k}^e\mathbf{u}^e = \mathbf{f}^e$, for the element. Applying the appropriate coordinate transformations, the element contributions can be assembled to form the global system of equations,

$$\mathrm{KU} = \mathrm{F}. \quad (8)$$

The matrix **K** depends on the shape functions and sensor locations, while **F** is only a function of the experimental strain measurements. The solution of Equation (8) requires the use of displacement boundary conditions to restrain the structure against rigid-body motion. Subsequently, matrix **K** is inverted, and the unknown nodal degrees of freedom, **U**, can be computed. In the case of small displacements, the sensor locations can be assumed to remain unchanged, and **K** is only required to be inverted once; this ensures the computational efficiency of iFEM in dynamic conditions, as **U** can be computed by only updating **F** at each strain-acquisition increment.

3 | EXPERIMENTAL CASE STUDY

The analysed structure is shown in Figures 1 and 2. It is made of beam and plate components joined together via bolted connections. Specifically, it consists of a rectangular fuselage and a single rectangular plate directly connected to the fuselage for realising the wings. Two shorter plate elements are applied at the wingtips to simulate the winglets. Finally, the model comprises similar plate elements to realise the vertical and the horizontal tail. It is built according to the Garteur benchmark project[7]; the main difference is that, for the fuselage, a thin-section Fe360 profile is used, with a length of 1.5 m and a thickness of 3.0 mm. The wingspan is 2.0 m, and the fuselage is 1.5 m long. The other elements, including the wings, are built using S235JRC+C steel plate elements, 8.0 mm thick and 100.0 mm wide.

The damage conditions have been simulated by applying additional masses (around 2% of the aeroplane mass), in two positions, as described in Delo et al.[23] In the first case, the simulated damage is applied on the left side of the horizontal tail; in the second case, the mass is applied on the left wing tip. When a structure experiences damage, its stiffness is locally altered. This result can be replicated in finite-element models by reducing the Young's modulus in specified regions.[24] Alternatively, discrete masses can be used, resulting in a straightforward and reversible method of modifying dynamic properties. This technique induces a decrease in eigenfrequency, which is equivalent to the effect of a local stiffness loss.[25,26] Therefore, a finite-element analysis has been performed, considering a simplified structural model using beam elements. This analysis helped defining an additional mass that, when applied on the wings, reduces the first natural frequency by an amount equivalent to a 50% reduction in the stiffness of elements placed in the same position as the mass over a length of 20 mm. The first natural frequency from the numerical model is 5.687 Hz in the undamaged condition and 5.632 Hz in the damaged condition, resulting in a 0.97% reduction, consistent with the experimental results in Table 6.

A broadband test is performed here, exciting the modes in the range of 0–50 Hz, using a periodic chirp input. The latter allows the FRFs and the SFRFs to be extracted. Subsequently, the structure is excited using the modal appropriation technique, trying to isolate the previously identified six lowest natural frequencies and to extract the corresponding mode shapes and strain responses along the fibre axis. The excitation is applied horizontally using a 7 lbf shaker with integrated amplifier, which is connected to the rear of the fuselage by means of a stinger (it can be seen in Figure 1).

The response is measured via a high-density 10-m-long fibre-optic sensor (HD6S), used with an ODiSI acquisition system, to provide more than a thousand distinct strain measurements per metre.[27] The sensor is glued to the surface of the structure, to measure the strains along the wings, on the trailing and leading edges and on the top and bottom surfaces. The fibre optic is subsequently fixed along the fuselage and also on the vertical and horizontal tail. The choice

FIGURE 1 Garteur laboratory-scale model and fibre-optic arrangement in the test configuration. The shaker is connected to the rear part of the fuselage, and the suspension system is located in the upper part.

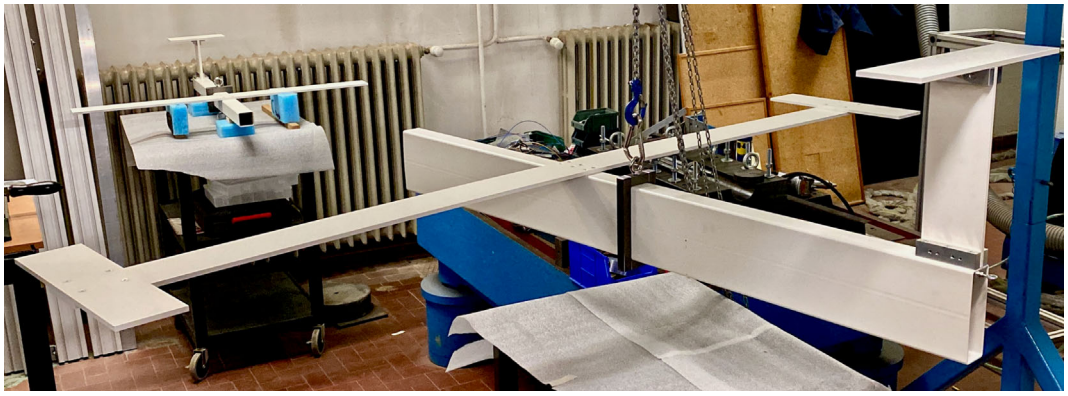

FIGURE 2 Garteur laboratory-scale model.

regarding sensor placement, shown in Figure 3, is intended to capture the main bending effects on the wings and tail according to the expected vibration modes and available instrumentation. A detailed study on optimal sensor patterns for iFEM can be found in Roy et al.[28] The iFEM shape-sensing technique is then adopted to reconstruct the full-field mode shapes from the strain time history responses, which can be compared to the ones extracted from the SLDV measurements. The velocity time history is simultaneously measured using the Polytec PSV-I-500 SLDV on a regular grid of 45 points.

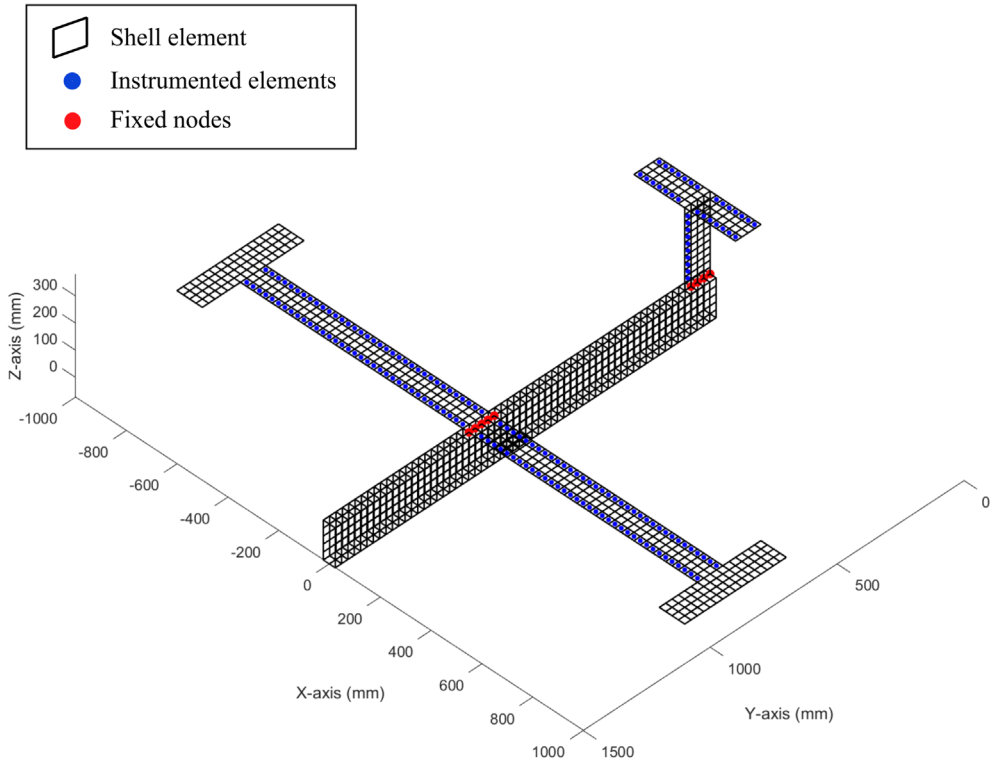

FIGURE 3 The iFEM model of the Garteur structure showing the instrumented elements and the boundary conditions.

TABLE 1 Details of the iFEM model and analysis.

Property	Value
Inverse shell element type	iQS4
Total number of shell elements	1400
Total number of nodes	1504
Number of elements instrumented with sensors	178
Number of fixed/clamped nodes	9
Value of weighting coefficient (uninstrumented elements)	10^{-5}

In the broadband test, the SLDV results are acquired using a sampling frequency of 250 Hz, 1600 spectral lines and three averages. Instead, in the modal appropriation approach, the SLDV velocity time history is measured using 1000 lines and three averages, and the response in the frequency domain is acquired using 800 spectral lines in the same frequency range. The strain time history is measured for 50 s, and the maximum sampling frequency, which is limited by the sensor length, is 100 Hz. The experimental tests have been carried out in the "LAQ-AERMEC Aeromechanical Structural Systems" laboratory of the Department of Mechanical and Aerospace Engineering, Politecnico di Torino.

The iFEM model of the Garteur structure is developed using the four-node inverse shell element (iQS4).[22] The inverse model is composed of 1400 inverse shell elements and is shown in Figure 3. Additional analysis details are provided in Table 1. The dynamic strains measured by the fibre-optic sensors are used as input for the iFEM analysis. Inverse elements with available experimental strain data are indicated in Figure 3. In these instrumented elements, only the component of strain longitudinal to the fibre (and measured at the element centroid) is used for the iFEM analysis, and the weights of Equation (6) are set to unity. For elements with no experimental data, the weights are set to a small value (10^{-5}). Shell elements on the wing use strains measured on both the top and bottom surfaces (see Equation 7). Instead, elements on the tail use strains measured only on the top surface. To avoid an analysis breakdown because of a significant number of uninstrumented elements, the inverse model of the wings and tail are analysed

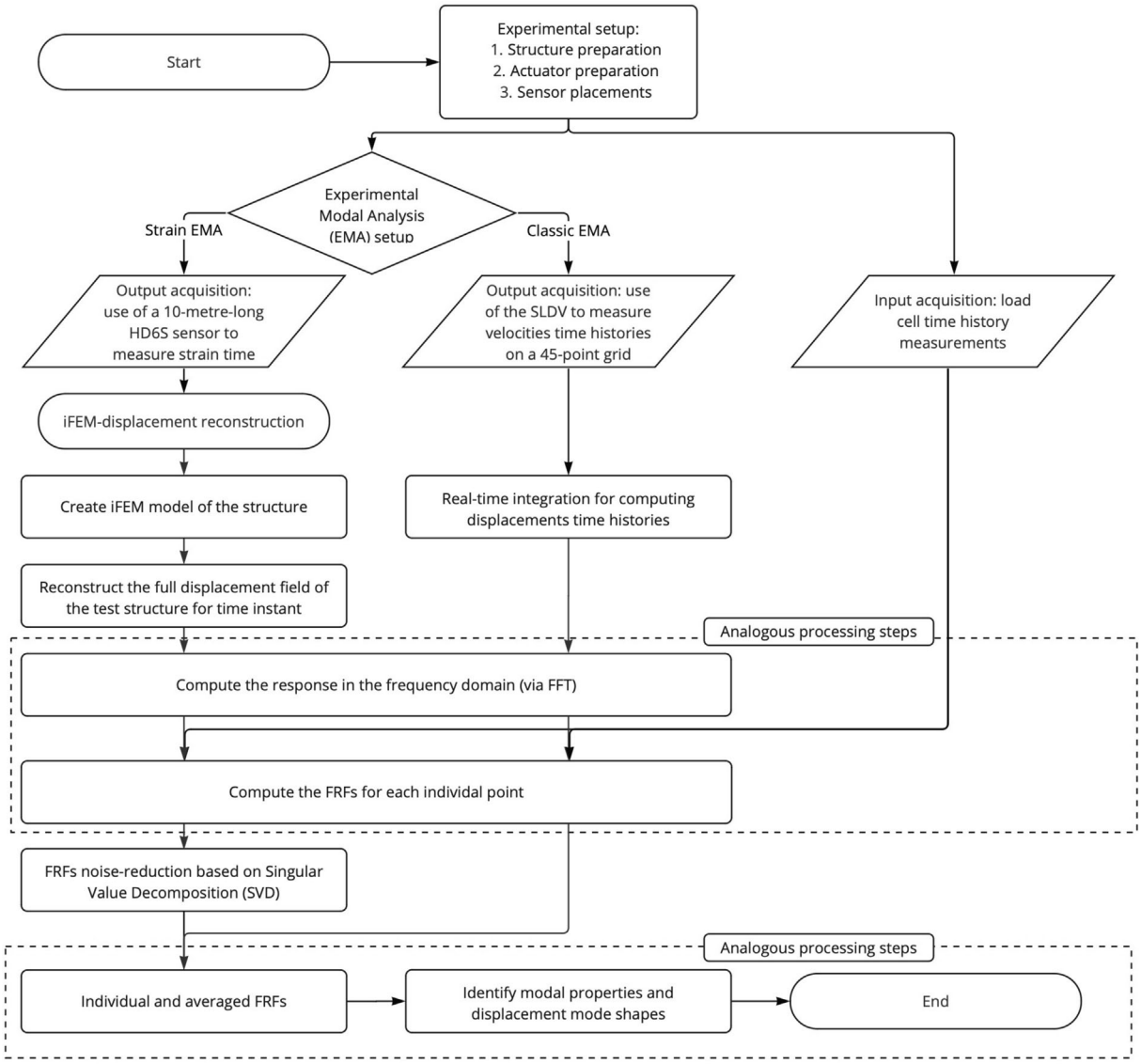

FIGURE 4 Flowchart of the classical and strain experimental modal analyses adopting iFEM for results harmonisation.

separately, with the results finally integrated into the complete model. Although the Garteur structure is unconstrained in the experimental tests, the iFEM analysis requires boundary conditions to ensure coherent results. Hence, considering the higher stiffness of the fuselage compared to the wings or tail, the nodes at the wing and tail root are assumed to be fixed (shown in Figure 3). Because of its high stiffness, the fuselage is likely to endure negligible deformations during excitation. Hence, the prescribed boundary condition is assumed to be a good approximation of the actual structural behaviour. The steps of the method to harmonise the strain and classical EMA using iFEM in each test configuration are collected in the flow chart shown in Figure 4. This flowchart highlights the specific phases required to perform strain-based EMA, that is, the displacement reconstruction performed for each time instant and the noise-reduction step. Additionally, Figure 4 shows some analogous processing steps to compute the FRFs based on the time history measurements and perform modal identification.

4 | RESULTS AND DISCUSSION

The following section presents the results of the strain EMA, the mode-shape sensing performed employing iFEM and the comparison with the SLDV modal displacements acquired using a broadband approach. The modal parameters are

identified, and the overall assessment is performed via the modal assurance criterion (MAC). Subsequently, the section presents the iFEM-reconstructed mode shapes and the SLDV modal displacements acquired using a modal appropriation approach.

4.1 | Broadband approach

The broadband EMA was performed in the range of 0–50 Hz, and the response was analysed in terms of the FRFs estimates of the SLDV displacements and the strain time history. The average spectra are shown in Figure 5 for the first damage condition analysed. The 50 Hz band was selected because it includes the main flexural and torsional vibration modes associated with the structure's wings. In addition, according to the Nyquist–Shannon theorem, it is possible to assess the SFRFs in this band as the maximum sampling frequency of the optical sensor is 100 Hz. The SLDV software includes real-time processing of the velocities to accurately provide displacements and accelerations time histories, via integration or differentiation of the velocity data. Subsequently, the displacements and the force reference signals are used to compute the H1 estimate of the displacement FRFs. Further details on the SLDV data processing can be found in Polytec.[29] The average spectrum is shown in Figure 5a. Similarly, it is possible to calculate the FRF estimate of the strain time history, shown in Figure 5b. It can be seen that the strain transfer function results are affected by noise. Consequently, a noise-reduction method based on singular value decomposition (SVD) is employed.[30]

This method analyses a single FRF, given as a vector $H = H_1, H_2, ..., H_L$, or its impulse response function (IRF) $h = h_1, h_2, ..., h_s$, where L is the number of spectral lines and $s = 2L$. In this study, IRF is used, as it guarantees a better performance of this method rather than directly considering the FRF.[30] The IRF is used to compute a Hankel matrix $[A]_{mxn}$, in which $A_{i,j} = h_{i+j-1}$ for $i = 1, ..., m$ and $j = 1, ..., n$ and $m + n - 1 = s$. It can be assumed that $[A] = [A]_r + [A]_n$, where $[A]_r$ is the uncontaminated matrix and $[A]_n$ is the noise contribution.

Consequently, from the SVD of the Hankel matrix, only the most significant singular values are used to reconstruct $[A]_r$ and the uncontaminated FRF. This approach depends on the determination of two parameters, that is, the dimension of the Hankel matrix and the rank r of the uncontaminated values in the SVD matrices, which is equivalent to the definition of a noise threshold. This rank is set as the number of values after which the IRF singular values reach an asymptotic behaviour. The smallest dimension of the Hankel matrix has to be higher than r, to include the effect of noise. Some spurious peaks are still present, yet the FRF results are overall less noisy. The strain data can be processed using a rank of 20 and the smallest dimension of $[A_r]$ equal to 200. The average spectrum computed from the filtered strain FRFs is shown in Figure 6.

The modal parameters are fitted using the least-squares complex exponential method from the SLDV and the strain FRFs. The impulse response of each FRF is fitted to a set of complex damped sinusoidal functions using Prony's method.[9,31] The adopted noise-decontamination method is similar to other methodologies that utilise data space

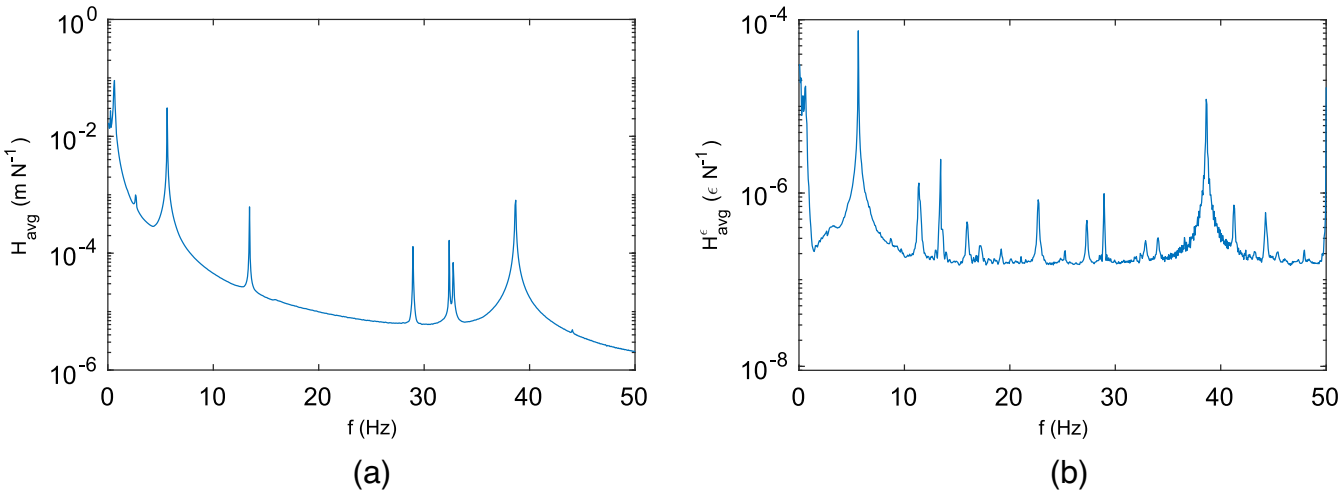

FIGURE 5 Average FRF spectra of the Garteur test structure in the range 0–50 Hz in the first damage condition analysed. (a) SLDV displacement FRF and (b) strain FRF.

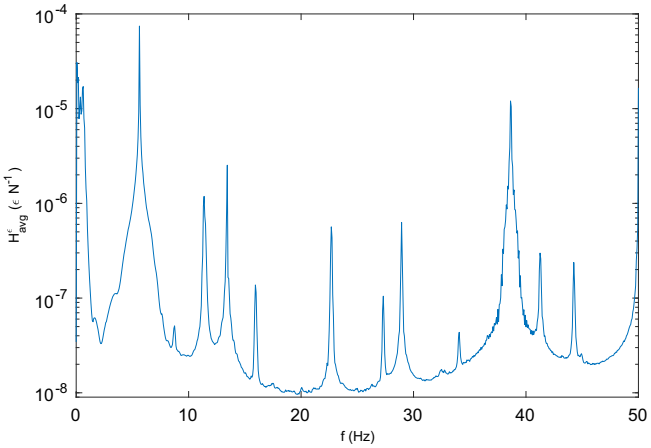

FIGURE 6 Average strain FRF spectrum of the Garteur test structure after filtering, in the first damage condition analysed.

decomposition via SVD, such as those related to stochastic subspace identification (SSI). These approaches aim to identify significant subspaces associated with the system's dynamic characteristics, such as natural frequencies and vibration modes. The use of these methods is highly beneficial when conducting operational modal analysis (OMA), as in the case of the covariance-driven stochastic subspace identification method (SSI-COV),[32] developed to identify modal parameters using time history of the ambient vibrations only. However, it may also be applied in the case of input–output measurement as shown in Li et al.[33] The numerical algorithm for Subspace State-Space System IDentification (N4SID), that also belongs to the class of SSI methods, is particularly similar to the approach presented earlier as it is based on subspace decomposition using the Hankel matrix. This algorithm can be used in both input-only and output-only cases. The quality of the results obtained from the algorithms can however be influenced by the initial choice of state-space model. Sensitivity to this choice may make a more careful analysis necessary. Although these SSI approaches were not required in the tests conducted by this study, they could be worthwhile for processing iFEM-reconstructed displacements in real-time dynamic monitoring, in the case of sensors embedded in in-service structures.

The identified parameters from the test under undamaged conditions are shown in Table 2. Consistent parameters are identified from both sensors, especially in terms of natural frequencies for Modes 1, 2, 3 and 6, which are all wing-bending vibration modes. However, as expected according to the optical sensor layout and the experimental setup, the torsional effects on the wings cannot be extracted. These modes, on the other hand, are correctly identified by the SLDV.

Analogously, it is possible to investigate the features of the simulated damage conditions.

The first damage condition, (DC1), regards the horizontal tail of the test structure. The identified modal parameters are shown in Table 3. By comparing the SLDV results in the normal and damage conditions, it is possible to highlight a shift in the natural frequencies. The error between the strain natural frequencies and the SLDV ones are generally low, except for the seventh mode, which is close to the maximum frequency that can be analysed with the strain sensor.

The results of the second damage condition, (DC2), are shown in Table 4. Similar to the first damage case, the shift in the natural frequencies is more evident from the SLDV results. It can be observed that, in the majority of cases, the results obtained from strain modal analysis are slightly inferior compared to those obtained from the classical approach.

The periodic chirp experimental results in the frequency domain also enable the mode shapes to be extracted. The DMSs are available on the 45 vibrometer scan point grid. These features are computed from the displacement FRFs adopting the least-squares complex exponential method, a least-squares estimation of the parameters associated with the vibration modes of the system, which is modelled by means of a combination of complex exponentials. The mode shapes are computed by minimising the difference between experimental data and the model. The measurements regard one direction only, that is, orthogonal to the wings' surface. Instead, the SMSs are available along the sensor axis. Figure 7 shows the DMSs in the three analysed conditions between the wingtips on the top surface. It can be observed how the bending mode shapes are affected by the presence of simulated damage in DC2, in which the additional mass is applied on the right wing. Analogously, it is possible to extract the SMSs. Figure 8 shows the SMSs along the wings, in the undamaged and damage conditions, processed with a moving average filter to remove spikes. Only the bending

TABLE 2 Modal parameters identified from SLDV displacement FRFs and strain FRFs and relative error between the natural frequencies.

	SLDV FRFs		Strain FRFs		
Mode	f_n (Hz)	ζ (-)	f_n (Hz)	ζ	**Relative error** $err(f_n)$ (%)
1	5.6423	0.0006	5.6223	0.0001	−0.3538
2	14.5866	0.0004	14.6100	0.0002	0.1605
3	29.8285	0.0003	29.8460	0.0023	0.0584
4	32.3907	0.0001	-	-	-
5	32.8007	0.0002	-	-	-
6	38.6979	0.0002	38.6890	0.0009	−0.0231
7	44.9811	0.0010	44.6377	0.0055	−0.7634

Note: The results are extracted from the tests performed in undamaged conditions.

TABLE 3 Modal parameters identified from SLDV displacement FRFs and strain FRFs and relative error between the natural frequencies.

	SLDV FRFs		Strain FRFs		
Mode	f_n (Hz)	ζ (-)	f_n (Hz)	ζ	**Relative error** $err(f_n)$ (%)
1	5.6329	0.0005	5.6327	0.0006	−0.0022
2	13.4315	0.0005	13.4286	0.0001	−0.0215
3	28.9483	0.0003	28.9394	0.0003	−0.0310
4	32.3802	0.0001	-	-	-
5	32.7694	0.0002	32.6144	0.0069	−0.4730
6	38.6594	0.0002	38.6545	0.0011	−0.0001
7	43.9600	0.0374	43.1474	0.0369	−1.8484

Note: The results regard the tests performed in the first damage condition.

TABLE 4 Modal parameters identified from SLDV displacement FRFs and strain FRFs and relative error between the natural frequencies.

	SLDV FRFs		Strain FRFs		
Mode	f_n (Hz)	ζ (-)	f_n (Hz)	ζ	**Relative error** $err(f_n)$ (%)
1	5.6337	0.0006	5.6323	0.0003	−0.0241
2	14.4372	0.0004	14.3703	0.0059	−0.4635
3	28.5384	0.0003	28.4836	0.0033	−0.1922
4	32.3795	0.0001	32.4067	0.0072	0.0838
5	32.6945	0.0003	-	-	-
6	37.4544	0.0002	37.4414	0.0005	−0.0347
7	44.8222	0.2395	45.0708	0.0099	0.5546

Note: The results regard the tests performed in the second damage condition.

modes can be identified. Specifically, the first and sixth mode shapes are clearer corresponding to the first modes of symmetric wing bending. Despite the noise in the input data, the effect of Damage Condition 2, where the damage is simulated on the right wing, can be discerned, especially from the first mode shape. The SMSs, in contrast to the displacement ones, can be reconstructed in different directions along the entire length of the fibre, as depicted in Appendix A. Thus, these functions also highlight the involvement of the tail in the vibration modes, which could be

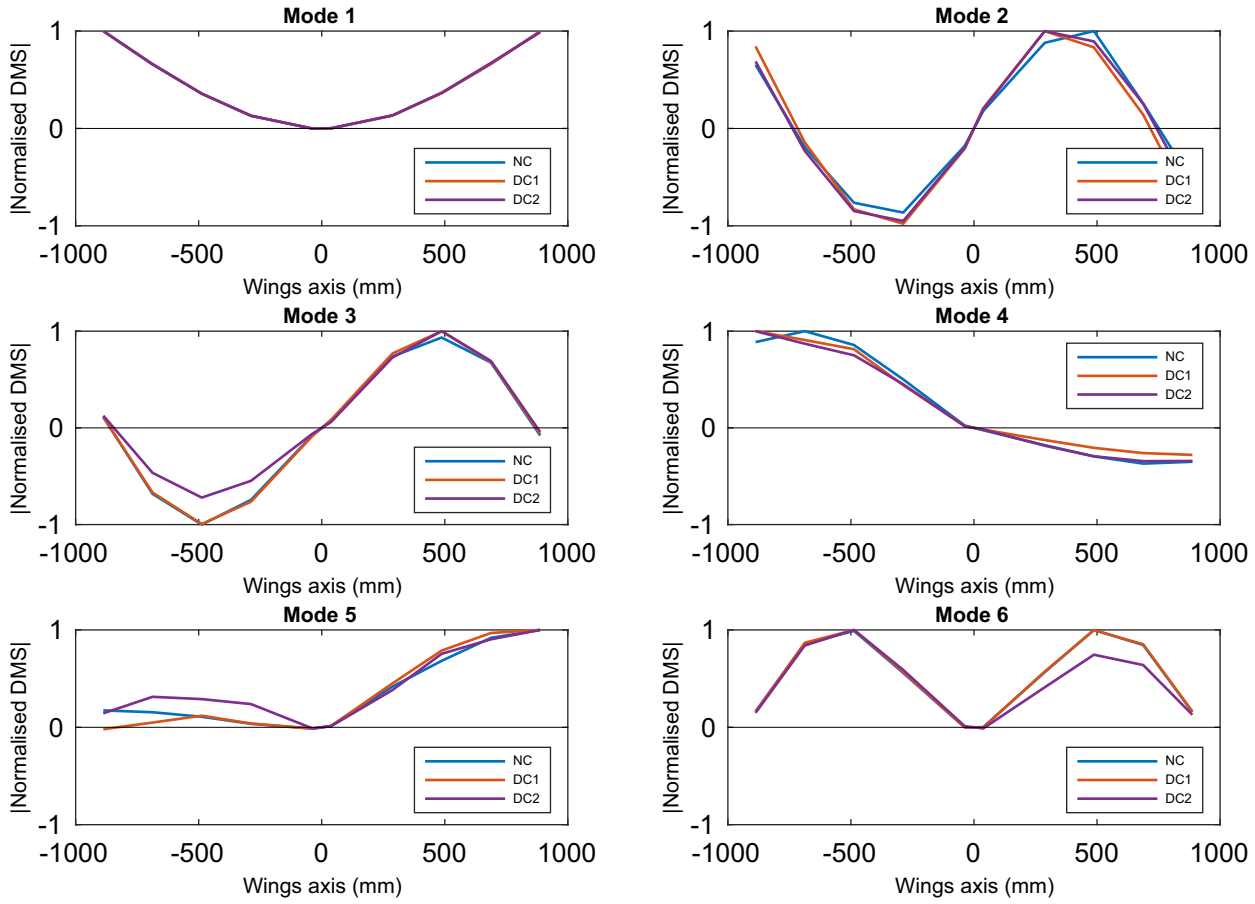

FIGURE 7 First six DMSs between the wingtips on the top surface. The mode shapes are extracted from SLDV measures in the normal condition and in the two damaged conditions.

used for monitoring additional damage locations on the test structure. Specifically, the bending of the vertical tail is observed in the second and third modes, which can be beneficial for detecting damage in that area. However, it can be observed that the data acquired under normal conditions are particularly noisy with respect to others. Therefore, the second and third SMSs cannot be distinctly extracted. This issue occurs particularly for the third mode shape, as can be noted in Figure 8. Instead, in the second mode shape, the strains are small in the central part of the wings, and the high noise causes a rapid decrease to zero in the SMS. The SMS variations induced in the damaged conditions are analysed by visually comparing the mode shapes and quantitatively comparing the MAC values between the two damaged cases and the undamaged case. The results are shown in Table 5.

The optic sensors in the current experimental configuration reproduce the mode shapes with a much higher density of points compared to the vibrometer. However, in the strain results, the signal noise must be filtered to estimate the shape, and torsional effects are not visible. Though, because of their higher density, these results enhance studying how damage affects the mode shapes of the test structure. In order to establish a direct comparison with the SLDV mode shapes and to ensure a higher homogeneity between the results of the two tests, the strain signal has been processed using the iFEM approach. This strategy has enabled the complete displacement field of the test structure to be reconstructed and utilised for the identification of the modal parameters.

The strain time history, acquired from the broadband excitation, has been employed as input in an inverse model of the structure, exploiting the iFEM formulation to obtain the displacement field. The displacements have been extracted specifically for the points corresponding to the grid measured by the SLDV. Subsequently, these signals have been processed similarly to the previous procedure. The FRFs have been computed (Figure 9). It can be noted that iFEM-reconstructed FRFs are consistent with the SLDV results and less noisy than the strain FRFs: This occurs because iFEM only considers strain values at specific points on the finite-element mesh and computes the displacements, leveraging the information given by all the strain data. In addition, enforcing the physical continuity of the displacements using

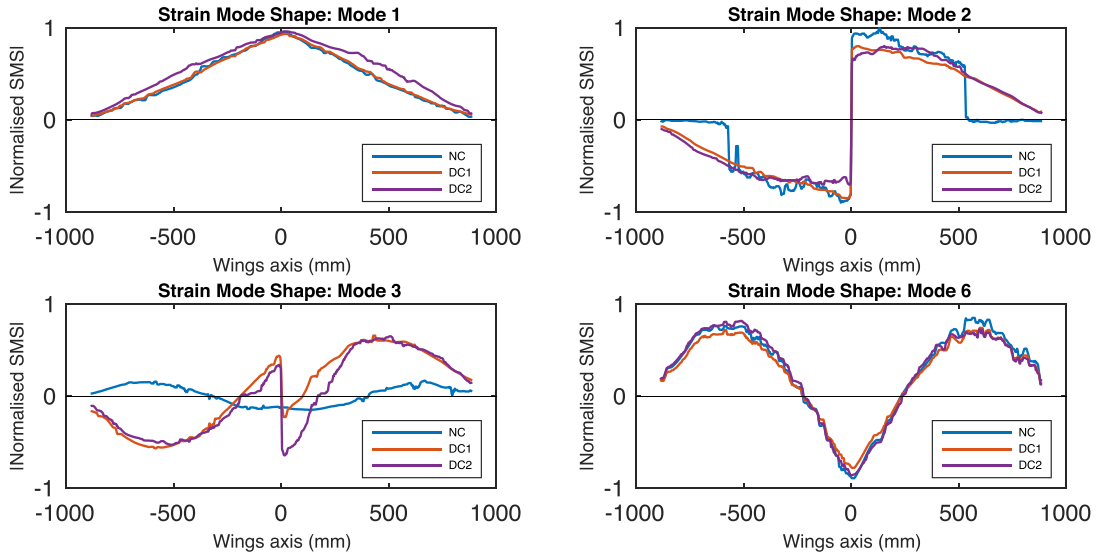

FIGURE 8 SMSs between the wingtips on the top surface, extracted from the strain measurements in the undamaged and damaged conditions.

TABLE 5 MAC values computed from the SMSs comparing the two damaged conditions with the undamaged condition.

Mode	Damaged Case 1 MAC	Damaged Case 2 MAC
1	0.9988	0.9809
2	0.8917	0.8711
4	0.9986	0.9900

the iFEM also contributes to the elimination of spurious peaks. The natural frequencies and damping ratios identified from the reconstructed displacements in the undamaged and damaged conditions as well as the relative changes in the natural frequencies are shown in Table 6.

It can be noted that the identified parameters are consistent with those obtained directly from the strain values, and the error with respect to the values obtained via SLDV is less than 1% for all bending modes. It is still difficult to identify torsional displacements, especially for the second damaged case. The main advantage is being able to derive the DMSs, which can be compared to the SLDV mode shapes using the MAC. These results are shown in Table 7.

The DMSs reconstructed using the iFEM approach do not allow for the identification of the coupling between the rotation of the fuselage around its axis and the bending of the wings. Therefore, in order to perform the comparison using the MAC, it is necessary to eliminate the rotation effect from the SLDV mode shapes, using the scan points on the joint between the fuselage and the wings as reference measurements to estimate the rigid motion components. Accordingly, all bending mode shapes are detectable based on the MAC values. In particular, the first and second modes always present a high coefficient in comparison with the reference DMSs. As for the third mode, likewise in the SMS case, the normal-condition mode shape cannot be identified. Conversely, in cases DC1 and DC2, the modal form is recognised, and good MAC values can be observed. This issue can be caused by the higher noise in the undamaged condition measurements and the difficulty of accurately extracting the properties, given the influence of the torsional modes at nearby frequencies. The MAC criterion can also find a match for the sixth mode, even if the coefficient is lower than the other bending modes. In this case, the FRF peaks and SMSs are identified. However, the iFEM-reconstructed DMSs are not equivalent to the reference DMSs. Specifically, the displacements are obtained using the inverse method over the entire structure mesh from the strains measurements. However, there are no available strain measurements on the winglets, and the extrapolation of displacements is less accurate: It induces a reduction in the MAC coefficient, calculated over the entire 45-point grid. It can be noted that, excluding the points on the winglets, the MAC coefficient increases from 0.5535 to 0.9648 in the undamaged case.

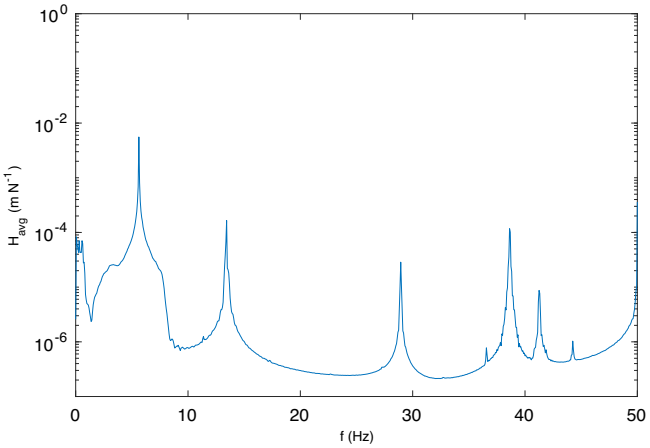

FIGURE 9 Average displacement FRF spectrum of the Garteur test structure, computed from the strain time histories using the iFEM approach, in the first damage condition analysed.

TABLE 6 Modal parameters identified from iFEM-reconstructed displacement FRFs.

	Undamaged case		Damaged Case 1			Damaged Case 2		
Mode	f_n **(Hz)**	ζ **(-)**	f_n **(Hz)**	ζ	$\delta(f_n)$ **(%)**	f_n **(Hz)**	ζ	$\delta(f_n)$ **(%)**
1	5.6855	0.0193	5.6317	0.0005	−0.95	5.6318	0.0003	−0.95
2	14.5795	0.0012	13.4293	0.0000	−7.89	14.4392	0.0002	−0.96
3	29.8770	0.0004	28.9246	0.0006	−3.19	28.5148	0.0010	−4.56
5	32.8003	0.0150	32.8435	0.0545	0.13	-	-	-
6	38.6539	0.0089	38.6775	0.0007	0.06	37.4557	0.0006	−3.1
7	43.8185	0.0005	44.2257	0.0044	0.94	44.5466	0.0162	1.66

TABLE 7 MAC comparison between the mode shapes identified from SLDV results and the ones identified from iFEM-reconstructed displacements.

Mode	**Undamaged case MAC**	**Damaged Case 1 MAC**	**Damaged Case 2 MAC**
1	0.9717	0.9994	0.9957
2	0.9896	0.9519	0.9891
3	0.1151	0.9145	0.9571
4	0.0323	0.0832	0.0003
5	0.0043	0.1573	0.0027
6	0.5535	0.5195	0.3445
7	0.0003	0.0735	0.0019

4.2 | Modal appropriation approach

The Garteur model was subsequently tested using sinusoidal excitation signals at the estimated natural frequencies (given in Table 2), to compute the normal mode shapes based on the modal appropriation method. This method is adopted to more effectively isolate the vibration modes of the test structure using the optical sensors and, consequently, verify the feasibility of employing the iFEM approach to reconstruct the entire DMSs.

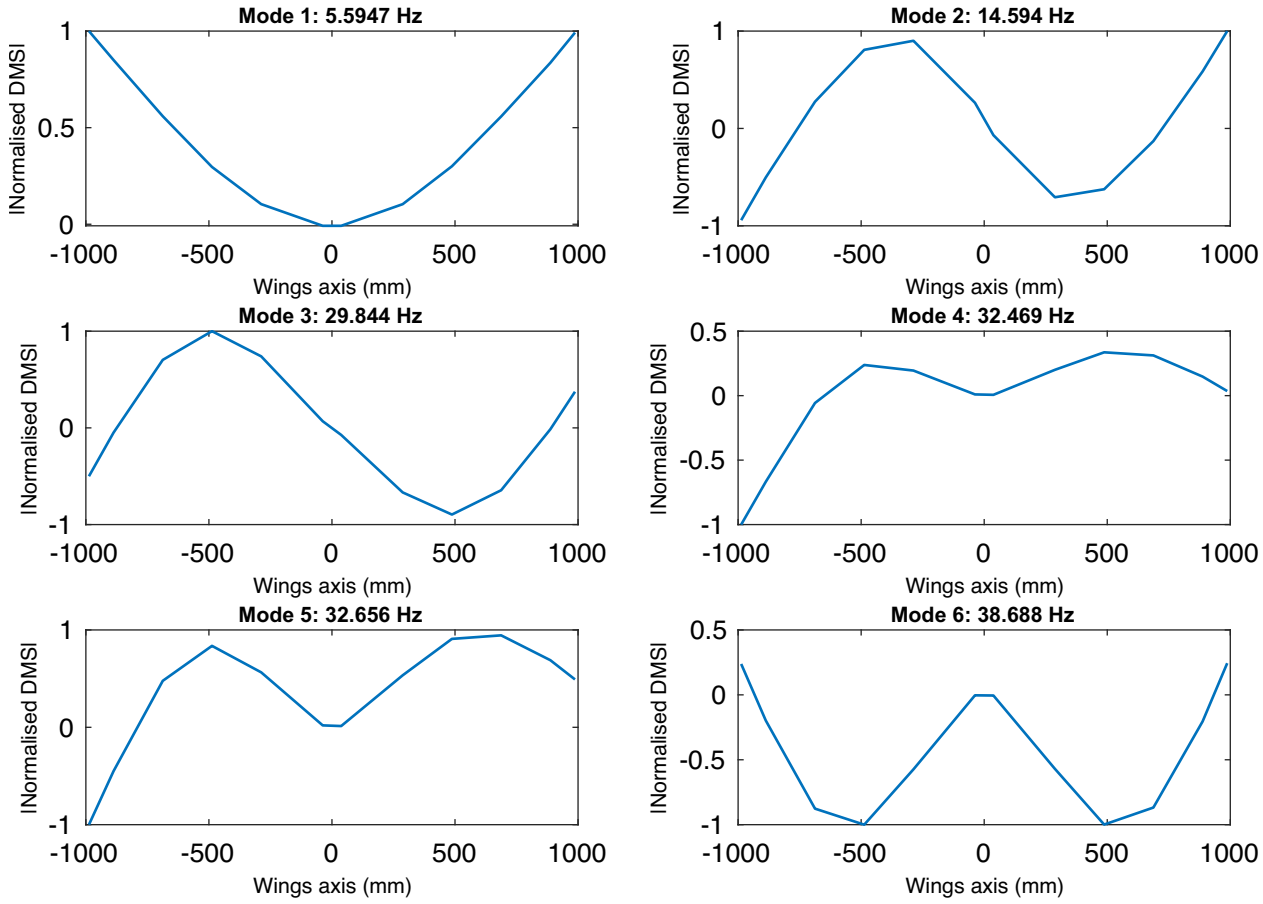

FIGURE 10 The first six DMSs along the wing leading edge estimated using the SLDV, using the modal appropriation technique.

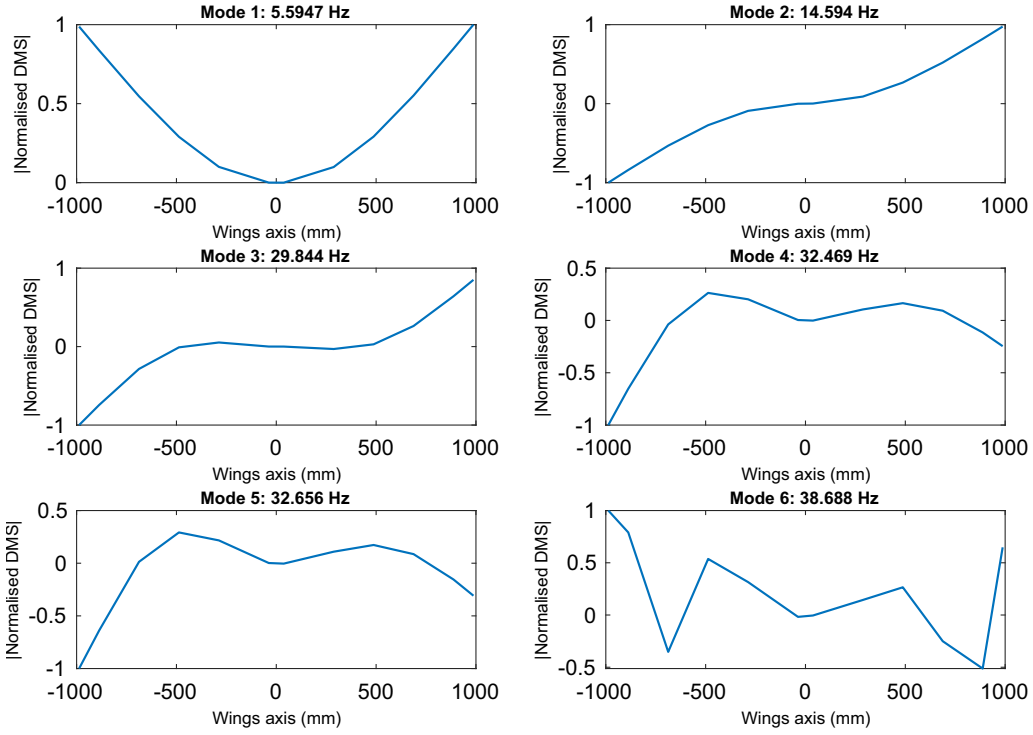

FIGURE 11 The first six DMSs along the wing leading edge estimated from the iFEM results, using the modal appropriation technique.

TABLE 8 Comparison of the MAC parameter between the first six mode shapes using the modal appropriation technique.

MAC	m_1^{iFEM}	m_2^{iFEM}	m_3^{iFEM}	m_4^{iFEM}	m_5^{iFEM}	m_6^{iFEM}
m_1^{vib}	0.965	0.000	0.006	0.529	0.565	0.363
m_2^{vib}	0.000	0.928	0.783	0.207	0.163	0.130
m_3^{vib}	0.000	0.893	0.981	0.287	0.232	0.123
m_4^{vib}	0.018	0.000	0.003	0.048	0.047	0.048
m_5^{vib}	0.033	0.001	0.000	0.049	0.057	0.107
m_6^{vib}	0.032	0.000	0.001	0.076	0.085	0.031

The SLDV and fibre-optic sensors are used to measure the system response. In these tests, the fibre-optic strains are measured at an acquisition frequency of 50 Hz for the first two natural modes and 100 Hz for the subsequent ones to optimise the signal-to-noise ratio of the measured data. At excitation frequencies greater than 30 Hz, the optical frequency domain reflectometry (OFDR) technique used by the fibre-optic sensor could not accurately compute strains at certain gauge points along the fibre. The high strain rate at these sites is the likely cause, and possible solutions involve using shorter length fibres and higher strain-acquisition frequencies. Regardless, these outlier data points were filtered out in the pre-processing stage. Subsequently, iFEM is used to compute the nodal-displacement time history from the measured strains.

The mode shapes corresponding to each excitation frequency are computed from the corresponding velocity and displacement FRFs and are shown in Figures 10 and 11. The mode shapes estimated from the SLDV measurements capture all six modes accurately. In contrast, those from the iFEM displacements are only accurate for the first three modes. The inaccuracy of Modes 4 and 5 is attributed to the limitation of iFEM in accurately reconstructing wing torsional deformation using a limited number of longitudinal strains. In the case of Mode 6, it is best explained by the noisy and incomplete strains measurements of the fibre sensor. The similarity of the strain and velocity-based modes shapes is determined using the MAC criterion, and the results are given in Table 8. As observed previously, the first three modes correlate very well, while the latter three do not. Additionally, the off-diagonal values are low, highlighting the orthogonality of the modes.

The torsional mode-shape sensing could be improved by altering the sensor configuration or changing the point of application of the external force, to increase the torsional response of the wings. Nevertheless, this strategy proves to be feasible even in the context of dynamic tests, capable of reconstructing characteristics comparable to the DMSs provided by the SLDV.

This experimental study shows the features that can be computed and analyses the differences between two different EMA approaches. Furthermore, the iFEM approach allows reconstructing the results in the same terms as those obtained with the SLDV. Hence, the harmonised features can be used in PBSHM to improve SHM performance via transfer-learning algorithms.

5 | CONCLUSIONS

This study focusses on the comparison between results and features gathered from fibre-optic strain sensors and SLDV, for examining the challenge of knowledge-transfer when the source and target datasets come from different sensors or experimental analyses.

These two approaches have been chosen because they provide high-density measurement points. Furthermore, despite some limitations, the fibre-optic strain sensors can represent a faster and cheaper solution in some operational scenarios. In addition, these strain measurements can be used as input in the iFEM methodology, enabling harmonisation of the features. Both types of sensors allow for performing EMA, accurately identifying the main modal parameters for the bending behaviour of the test structure.

The tests were carried out considering two different types of excitation and were repeated in the undamaged configuration and simulating damage in two locations, on the tail and the wing. The strain signals are processed to reduce the effect of noise, and the system parameters are identified. The natural frequencies can be identified from both sensor responses by applying a broadband excitation, and the average relative errors are less than 1%. However, the damping

factor is effectively computed only in the classical approach since the results obtained from the optical sensor, being particularly noisy, do not allow for optimal estimation of these parameters. Mode shapes can be extracted from both types of EMA. SLDV measurements can be used to directly extract DMSs on the grid of measured points, while strain measurements can be used for computing the SMSs along the fibre length. The second option could provide valuable insight into the tail contribution and for detecting any changes because of damage. In addition, via iFEM, it is also possible to recover mode shapes in terms of displacement from the strain data.

Globally, the SLDV modal analysis provides more comprehensive results in terms of DMSs, while the fibre-optic sensor offered a spatially denser response, although in a limited frequency range. Furthermore, the iFEM technique reconstructed the displacement response for the entire mesh of the numerical model. This approach can be useful for obtaining the displacement response at specific points, allowing for harmonising different experimental results. Additionally, the higher measurement point density in the SMSs enables a greater sensitivity to damage identification. The comparison between the SLDV and iFEM DMSs is carried out via the MAC, which highlights a satisfactory performance for the first three bending modes.

The results of the modal appropriation and the broadband techniques also validate the possibility of employing the iFEM shape-sensing technique for dynamic tests. One notable advantage is iFEM's ability to reconstruct the displacements across the entire structure, as opposed to solely in specific locations and in a single direction, which is a limit of SLDV results. It can be observed that the bending mode shapes have been identified, particularly for the first three modes. Yet, the MAC value is lower for the sixth mode because of decreased accuracy in the reconstruction of winglet displacements, as there are no strain measurements at those points. Moreover, identifying torsional vibration modes from the results of the strain modal analysis remains challenging. Nevertheless, to further investigate torsional effects, it would be possible to extend the tests by introducing additional sensors, such as triaxial strain gauges, which would improve the shape-sensing results. In addition, it would be possible to use shorter fibre-optic sensors to improve the signal quality in a broader frequency range, as the maximum sampling frequency could be increased.

Sharing knowledge between these tests could be exploited to address the challenges of the noisy nature of optical sensor data and the difficulty of identifying torsional vibration modes and extracting more sensitive features. Further developments could investigate the possibility of applying transfer-learning approaches, by training a model on SLDV data and then fitting them to fibre-optic sensor strain data, improving the generalisation capability of the model. In addition, in the context of PBSHM, it would be interesting to use data from multiple sensors as sources, to further improve diagnostic inferences on a different target, for which only a few experimental results are available.

ACKNOWLEDGEMENTS

The authors of this paper gratefully acknowledge the support of the UK Engineering and Physical Sciences Research Council (EPSRC) via grant references EP/W005816/1 and EP/S001565/1.

DATA AVAILABILITY STATEMENT

The data that support the findings of this study are available from the corresponding author upon reasonable request.

ORCID

Giulia Delo https://orcid.org/0000-0003-3502-3045
Rinto Roy https://orcid.org/0000-0003-4954-0166
Keith Worden https://orcid.org/0000-0002-1035-238X
Cecilia Surace https://orcid.org/0000-0002-3993-9432

REFERENCES

[1] P. Gardner, X. Liu, K. Worden, *Mech. Syst. Signal Process.* **2020**, *138*, 106550. https://doi.org/10.1016/j.ymssp.2019.106550
[2] L. Bull, P. Gardner, J. Gosliga, T. Rogers, N. Dervilis, E. Cross, E. Papatheou, A. Maguire, C. Campos, K. Worden, *Mech. Syst. Signal Process.* **2021**, *148*, 107141.
[3] J. Gosliga, P. Gardner, L. Bull, N. Dervilis, K. Worden, *Mech. Syst. Signal Process.* **2021**, *148*, 107144.
[4] P. Gardner, L. A. Bull, J. Gosliga, N. Dervilis, K. Worden, *Mech. Syst. Signal Process.* **2021**, *149*, 107142.
[5] L. Yam, T. Leung, K. Xue, B. Wang, D. Li, *Proc. 12th Int. Modal Anal.* **1994**, *2251*, 1415.
[6] M. Gherlone, P. Cerracchio, M. Mattone, *Prog. Aerosp. Sci.* **2018**, *99*, 14. https://doi.org/10.1016/j.paerosci.2018.04.001

[7] M. Link, M. Friswell, *Mech. Syst. Signal Process.* **2003**, *17*(1), 9. https://doi.org/10.1006/mssp.2002.1534
[8] G. Delo, A. Bunce, E. Cross, J. Gosliga, D. Hester, C. Surace, K. Worden, D. Brennan, *European Workshop on Structural Health Monitoring*, EWSHM **2022**. Lecture Notes in Civil Engineering (Eds: P. Rizzo, A. Milazzo), Vol 254. Springer, Cham 2023. https://doi.org/10.1007/978-3-031-07258-1_97
[9] D. Ewins, *Modal Testing: Theory, Practice and Application*, Mechanical Engineering Research Studies: Engineering Dynamics Series, John Wiley & Sons Ltd., West Sussex, England **2009**.
[10] O. Bernsconi, D. Ewins, *Analysis* **1989**, *4*(2), 68.
[11] L. Yam, T. Leung, D. Li, K. Xue, *J. Sound Vib.* **1996**, *191*(2), 251. https://doi.org/10.1006/jsvi.1996.0119
[12] J. M. López-Higuera, L. R. Cobo, A. Q. Incera, A. Cobo, *J. Lightwave Technol.* **2011**, *29*(4), 587.
[13] M. A. Davis, A. D. Kersey, J. Sirkis, E. J. Friebele, *Smart Mater. Struct.* **1996**, *5*(6), 759. https://doi.org/10.1088/0964-1726/5/6/005
[14] H.-Y. Ling, K.-T. Lau, L. Cheng, *Comp. Struct.* **2004**, *66*(1–4), 317. https://doi.org/10.1016/j.compstruct.2004.04.054
[15] A. Paolozzi, P. Gasbarri, *Multifunctional Structures/Integration of Sensors and Antennas*, NATO-RTO-AVT, Vilnius, Lituania **2006** 9.1.
[16] T. Kranjc, J. Slavič, M. Boltežar, *J. Vib. Control.* **2016**, *22*(2), 371.
[17] F. Shadan, F. Khoshnoudian, A. Esfandiari, *Int. J. Struct. Stab. Dyn.* **2018**, *18*(12), 1850159.
[18] R. Roy, M. Gherlone, C. Surace, *Aerosp. Sci. Technol.* **2021**, *110*, 106484. https://doi.org/10.1016/j.ast.2020.106484
[19] A. Tessler, *A Variational Principle for Reconstruction of Elastic Deformations in Shear Deformable Plates and Shells*, National Aeronautics and Space Administration, Langley Research Center, Hampton, VA **2003**.
[20] A. Tessler, J. L. Spangler, *Comput. Methods Appl. Mech. Eng.* **2005**, *194*(2–5), 327.
[21] R. Roy, A. Tessler, C. Surace, M. Gherlone, *Thin-Walled Struct.* **2022**, *180*, 109798. https://doi.org/10.1016/j.tws.2022.109798
[22] A. Kefal, E. Oterkus, A. Tessler, J. L. Spangler, *Eng. Sci. Technol Int. J.* **2016**, *19*(3), 1299. https://doi.org/10.1016/j.jestch.2016.03.006
[23] G. Delo, M. Mattone, C. Surace, K. Worden, presented at XII Int. Conf. on Structural Dynamics (EURODYN 2023), 02–05 July 2023, Delft, The Netherlands, **2023**.
[24] M. Friswell, J. Penny, S. Garvey, *Comput. Struct.* **1998**, *69*(5), 547. https://doi.org/10.1016/S0045-7949(98)00125-4
[25] E. Papatheou, G. Manson, R. J. Barthorpe, K. Worden, *J. Sound Vib.* **2010**, *329*(12), 2349. https://doi.org/10.1016/j.jsv.2009.07.020
[26] I. Behmanesh, B. Moaveni, *Struct. Control Health Monit.* **2015**, *22*(3), 463.
[27] Luna Inc. HD strain sensors. High-definition fiber optic strain sensors. https://www.lunainc.com
[28] R. Roy, A. Tessler, C. Surace, M. Gherlone, *Sensors* **2020**, *20*(24), 7049. https://doi.org/10.3390/s20247049
[29] Polytec. PSV-500 scanning vibrometer. Full-field vibration measurement. Datasheet. https://www.polytec.com
[30] K. Sanliturk, O. Cakar, *Mech. Syst. Signal Process.* **2005**, *19*(3), 615.
[31] R. Prony, *J. de l'Ecole Polytech.* **1795**, *1*, 24.
[32] E. Cheynet. Operational modal analysis with automated SSI-COV algorithm. **2020**. https://doi.org/10.5281/ZENODO.3774061. https://zenodo.org/record/3774061
[33] P. Li, T. Zhao, J. Zhang, J. Wei, M. Q. Feng, D. Feng, S. Li, *Comput. Aided Civ. Inf. Eng.* **2023**, *38*(13), 1789.

How to cite this article: G. Delo, R. Roy, K. Worden, C. Surace, *Strain* **2024**, e12481. https://doi.org/10.1111/str.12481

APPENDIX A

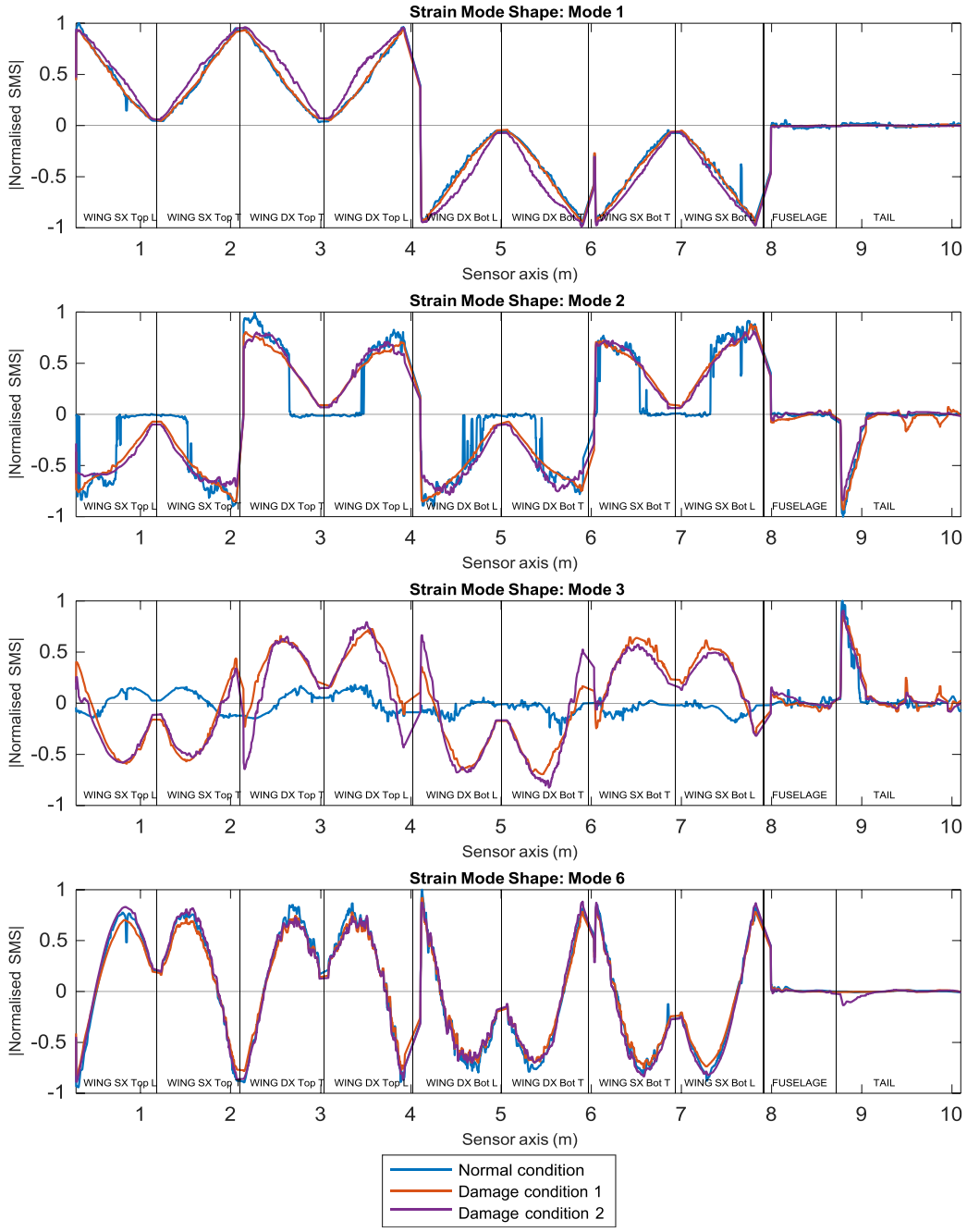

FIGURE A1. Strain mode shapes (SMSs) along the fibre-optic sensor axis, extracted from the strain measurements in the undamaged and damaged conditions. The structure sections for each segment of the fibre-optic sensor are indicated. The optical fibre is initially laid on the two wings, on the top and bottom surfaces, on the leading and trailing edges of the wings. Subsequently, the fibre is applied on the fuselage, on the vertical section of the tail and finally on the horizontal part of the tail. SMSs can be evaluated for the bending mode shapes, that is, 1, 2, 3 and 6.